

RESOLVING THE FORMATION OF PROTOGALAXIES. II. CENTRAL GRAVITATIONAL COLLAPSE

JOHN H. WISE^{1,2}, MATTHEW J. TURK¹, AND TOM ABEL¹

Draft version October 11, 2007

ABSTRACT

Numerous cosmological hydrodynamic studies have addressed the formation of galaxies. Here we choose to study the first stages of galaxy formation, including non-equilibrium atomic primordial gas cooling, gravity and hydrodynamics. Using initial conditions appropriate for the concordance cosmological model of structure formation, we perform two adaptive mesh refinement simulations of $\sim 10^8 M_\odot$ galaxies at high redshift. The calculations resolve the Jeans length at all times with more than 16 cells and capture over 14 orders of magnitude in length scales. In both cases, the dense, 10^5 solar mass, one parsec central regions are found to contract rapidly and have turbulent Mach numbers up to 4. Despite the ever decreasing Jeans length of the isothermal gas, we only find one site of fragmentation during the collapse. However, rotational secular bar instabilities transport angular momentum outwards in the central parsec as the gas continues to collapse and lead to multiple nested unstable fragments with decreasing masses down to sub-Jupiter mass scales. Although these numerical experiments neglect star formation and feedback, they clearly highlight the physics of turbulence in gravitationally collapsing gas. The angular momentum segregation seen in our calculations plays an important role in theories that form supermassive black holes from gaseous collapse.

Subject headings: cosmology: theory — galaxies: formation — black holes: formation — secular instability

1. MOTIVATION & PREVIOUS WORK

Since the first investigations of galaxy interactions (Holmberg 1941) using light bulbs, the use of numerical simulations in galaxy formation has developed dramatically. Not only gravity but also hydrodynamics and cooling are standard ingredients in the sophisticated computer models studying galaxy formation and interactions. In hierarchical structure formation, dark matter (DM) halos merge to form larger halos while the gas infalls into these potential wells (Peebles & Dicke 1968; White & Rees 1978). White & Rees provided the basis for modern galaxy formation, in which small galaxies form early and continuously merge into larger systems.

As more high redshift galaxies were observed in the following 10 years, White & Frenk (1991) refined the theory to address the observed characteristics in these galaxies. In their model, the halo accumulates mass until the gas cools faster than a Hubble time, t_H , which usually occurs when atomic hydrogen line, specifically Ly α , cooling is efficient. This happens when the halo has $T_{\text{vir}} > 10^4$ K, where the cooling function sharply rises by several orders of magnitude because the number of free electrons able to excite hydrogen greatly increases at this temperature (Spitzer 1978). One can define a cooling radius, r_{cool} , in which the interior material is able to cool within a Hubble time. Once the halo reaches this first milestone, r_{cool} increases through additional accretion and cooling. A rapid baryonic collapse ensues when $t_{\text{cool}} \lesssim t_{\text{dyn}}$ (Rees & Ostriker 1977). The material accelerates towards the center, and its density quickly increases. In the model discussed in White & Frenk, this collapse will halt when one of the following circumstances occurs. First, angular

momentum can prevent the gas from collapsing further, and the system becomes rotationally supported. Afterwards, this disc fragments and star formation follows. Alternatively, star formation does not necessarily develop in a disc component, but the energy released by stars during their main sequence and associated supernovae (SNe) terminates the collapse.

These concepts have been applied also to the earliest galaxies in the universe (Mo et al. 1998; Oh & Haiman 2002; Begelman et al. 2006; Lodato & Natarajan 2006). Many studies (e.g. Ostriker & Gnedin 1996; Haiman et al. 1997; Cen 2003; Somerville & Livio 2003; Wise & Abel 2005) demonstrated that OB-stars within protogalaxies at $z > 6$ can produce the majority of photons required for reionization. These protogalaxies contain an ample gas reservoir for widespread star formation, and the accompanying radiation propagates into and ionizes the surrounding neutral intergalactic medium. Several high redshift starburst galaxies have been observed that host ubiquitous star formation at $z > 6$ (Stanway et al. 2003; Mobasher et al. 2005; Bouwens et al. 2006). Additionally, supermassive black holes (SMBH) more massive than $10^8 M_\odot$ are present at these redshifts (e.g. Becker et al. 2001; Fan et al. 2002, 2006). Finally, a reionization signature in the polarization of the cosmic microwave background (CMB) at $z \sim 10$ (Page et al. 2007) further supports and constrains stellar and SMBH activity at high redshifts.

The distinction between SMBH formation and a starburst galaxy should depend on the initial ingredients (i.e. seed BHs, metallicity, merger histories) of the host halo, but the evolution of various initial states is debatable. It is essential to study the hydrodynamics of high redshift halo collapses because the initial luminous object(s) that emerges will dynamically and thermally alter its surroundings. For example, as the object emits ultraviolet radiation, the nearby gas heats and thus the characteris-

Electronic address: john.h.wise@nasa.gov

¹ Kavli Institute for Particle Astrophysics and Cosmology, Stanford University, Menlo Park, CA 94025

² Current address: Laboratory for Observational Cosmology, NASA Goddard Space Flight Center, Greenbelt, MD 21114

tic Jeans mass increases, which may inhibit the accretion of new gas for future star formation (Efstathiou 1992; Thoul & Weinberg 1996).

The following work will attempt to clarify early galaxy formation by focusing on protogalactic ($T_{\text{vir}} > 10^4$ K) halos and following their initial gaseous collapse. Wise & Abel (2007, hereafter Paper I) studied the virialization of protogalactic halos and the virial generation of supersonic turbulence. In this paper, we address the gas dynamics of the continued, turbulent collapse of a halo and study the evolution and characteristics of the central regions. In later studies, we will introduce the effects from primordial star formation and feedback and H_2 cooling. The progressive introduction of new processes is essential to understand the relevance of each mechanism. We argue that our results may be relevant for scenarios that envisage SMBH formation from gaseous collapses.

Loeb & Rasio (1994) and Bromm & Loeb (2003) conducted smoothed particle hydrodynamics (SPH) simulations that focused on the collapse of idealized, isolated protogalactic halos. The former group concluded that a central $10^6 M_\odot$ SMBH must exist to stabilize the thin gaseous disc that forms in their calculations. Bromm & Loeb considered cases with and without H_2 chemistry and a background UV radiation field. They observed the formation of a dense object with a mass $M \sim 10^6 M_\odot$, or $\gtrsim 10\%$ of the baryonic matter, in simulations with no or strongly suppressed H_2 formation. These calculations without metal cooling and stellar feedback are useful to explore the hydrodynamics of the collapse under simplified conditions. Spaans & Silk (2006) analytically studied the collapse of 10^4 K halos with an atomic equation of state. They find that $\sim 0.1\%$ of the baryonic mass results in a pre-galactic BH with a mass $\sim 10^5 M_\odot$. Lodato & Natarajan (2006) also found that $\sim 5\%$ of the gas mass in $M = 10^7 M_\odot$ halos at $z \sim 10$ becomes unstable in a gaseous disc and forms a SMBH. Recently, Clark et al. (2007) studied the effects of metal and dust cooling on the fragmentation of a collapsing protogalactic core with varying metallicities ($Z = 0, 10^{-6}, 10^{-5} Z_\odot$) and found the gas fragmenting ten times as much in the $10^{-5} Z_\odot$ case than the primordial case. In addition, the fragments in the primordial case are biased toward larger masses.

A runaway gaseous collapse requires angular momentum transport so material can inflow to small scales and form a central object. The stability of rotating gaseous clouds have been subject of much interest over the last four centuries and was thoroughly detailed by the work of Chandrasekhar (1969, hereafter EFE). In the 1960's and 1970's, studies utilizing virial tensor techniques (EFE; Lebovitz 1967; Ostriker & Tassoul 1969; Ostriker & Bodenheimer 1973), variational techniques (Lynden-Bell & Ostriker 1967; Bardeen et al. 1977), and N-body simulations (Ostriker & Peebles 1973) all focused on criteria in which a stellar or gaseous system becomes secularly or dynamically unstable. The first instability encountered is an $m = 2$ bar-like instability that is conducive for angular momentum transport in order to form a dense, central object. Begelman et al. (2006) investigated the conditions where a gaseous disc in a pre-galactic halo would become rotationally unstable to bar formation (see Christodoulou et al. 1995a,b). They adapt the ‘‘bars within bars’’ scenario (Shlosman et al. 1989, 1990), which was originally formulated to drive SMBH accretion from

a gaseous bar that forms within a stellar galactic bar, to the scenario of pre-galactic BH formation. Here a cascade of bars form and transport angular momentum outwards, and the system can collapse to small scales to form a quasistar with runaway neutrino cooling, resulting in a central SMBH. The simulations detailed below show how much central bar-like instabilities form.

In §2, we describe our simulations and their cosmological context. In the following section, we present our analysis of the halo collapse simulations and investigate the structural and hydrodynamical evolution, the initial halo collapse, rotational instabilities, and the importance of turbulence. In §4, we discuss the relevance of angular momentum transport and rotational instabilities in early galaxy and SMBH formation. There we also examine the applicability and limitations of our results and desired improvements for future simulations. Finally we conclude in the last section.

2. SIMULATION TECHNIQUES

To investigate protogalactic halo collapses in the early universe, we utilize an Eulerian structured, adaptive mesh refinement (AMR), cosmological hydrodynamical code, *Enzo*³ (Bryan & Norman 1997, 1999; O’Shea et al. 2004). *Enzo* solves the hydrodynamical equations using a second order accurate piecewise parabolic method (Woodward & Colella 1984; Bryan et al. 1994), while a Riemann solver ensures accurate shock capturing with minimal viscosity. Additionally *Enzo* uses a particle-mesh N-body method to calculate the dynamics of the collisionless dark matter particles (Couchman 1991). Regions of the simulation grid are refined by two when one or more of the following conditions are met: (1) Baryon density is greater than 3 times $\Omega_b \rho_0 N^{l(1+\phi)}$, (2) DM density is greater than 3 times $\Omega_{\text{CDM}} \rho_0 N^{l(1+\phi)}$, and (3) the local Jeans length is less than 16 cell widths. Here $N = 2$ is the refinement factor; l is the AMR refinement level; $\phi = -0.3$ causes more frequent refinement with increasing AMR levels, i.e. super-Lagrangian behavior; $\rho_0 = 3H_0^2/8\pi G$ is the critical density; and the Jeans length, $L_J = \sqrt{15kT/4\pi\rho G\mu m_H}$, where H_0 , k , T , ρ , μ , and m_H are the Hubble constant, Boltzmann constant, temperature, gas density, mean molecular weight in units of the proton mass, and hydrogen mass, respectively. The Jeans length refinement insures that we meet the Truelove criterion, which requires the Jeans length to be resolved by at least 4 cells on each axis (Truelove et al. 1997). Runs with a refinement criterion of 4, 8, and 16 Jeans lengths have indistinguishable mass weighted radial profiles.

We conduct the simulations within the concordance Λ CDM model with WMAP 1 year parameters of $h = 0.72$, $\Omega_\Lambda = 0.73$, $\Omega_M = 0.27$, $\Omega_b = 0.024h^{-2}$, and a primordial scale invariant ($n = 1$) power spectrum with $\sigma_8 = 0.9$ (Spergel et al. 2003). h is the Hubble parameter in units of $100 \text{ km s}^{-1} \text{ Mpc}^{-1}$. Ω_Λ , Ω_M , and Ω_b are the fractions of critical energy density of vacuum energy, total matter, and baryons, respectively. σ_8 is the rms of the density fluctuations inside a sphere of radius $8h^{-1} \text{ Mpc}$. Using the WMAP1 parameters versus the significantly different WMAP third year parameters (WMAP3;

³ See <http://lca.ucsd.edu/software/enzo/>

TABLE 1
SIMULATION PARAMETERS

Name	l [Mpc]	N_{part}	N_{grid}	N_{cell}	L_{max}	Δx [R_{\odot}]
A	1.0	2.22×10^7	44712	1.23×10^8 (498 ³)	41	9.3×10^{-3}
B	1.5	1.26×10^7	22179	7.40×10^7 (420 ³)	41	1.4×10^{-2}

NOTE. — Col. (1): Simulation name. Col. (2): Number of dark matter particles. Col. (3): Number of AMR grids. Col. (4): Maximum number of unique grid cells. Col. (5): Maximum level of refinement reached in the simulation. Col. (6): Resolution at the maximum refinement level.

TABLE 2
HALOS OF INTEREST^a

l [Mpc]	z	M_{tot} [M_{\odot}]	σ	ρ_c [cm^{-3}]	T_c [K]	M_{BE} [M_{\odot}]
1.0	15.87	3.47×10^7	2.45	5.84×10^{21}	8190	4.74×10^5
1.5	16.80	3.50×10^7	2.59	7.58×10^{21}	8270	1.01×10^5

NOTE. — Col. (1): Box size of the simulation. Col. (2): Final redshift of simulation. Col. (3): Total halo mass. Col. (4): σ of the total mass compared to matter fluctuations. Col. (5): Central halo density. Col. (6): Central gas temperature. Col. (7): Gravitationally unstable central mass.

^aThe subscript “c” denotes central quantities.

Spergel et al. 2007) have no effect on the evolution of individual halos that are considered here (see Paper I for more discussion). The initial conditions of this simulation are well-established by the primordial temperature fluctuations in the cosmic microwave background (CMB) and big bang nucleosynthesis (BBN) (Burles et al. 2001; Hu & Dodelson 2002, and references therein).

We perform two realizations in which we vary the box size and random phase to study different scenarios and epochs of halo collapse. In the first simulation, we setup a cosmological box with 1 comoving Mpc on a side (simulation A), periodic boundary conditions, and a 128^3 top grid. The other simulation is similar but with a box side of 1.5 comoving Mpc and a different random phase (simulation B). We provide a summary of the simulation parameters in Table 1. These volumes are adequate to study halos of interest because the comoving number density of $>10^4$ K halos at $z = 10$ is $\sim 6 \text{ Mpc}^{-3}$ according to an ellipsoidal variant of Press-Schechter formalism (Sheth & Tormen 2002). We use the COSMICS package to calculate the initial conditions⁴ at $z = 129$ (119) (Bertschinger 1995, 2001). It calculates the linearized evolution of matter fluctuations. We first run a dark matter simulation to $z = 10$ and locate the DM halos using the HOP algorithm (Eisenstein & Hut 1998). We identify the first dark matter halo in the simulation that has $T_{\text{vir}} > 10^4$ K and generate three levels of refined, nested initial conditions with a refinement factor of two that are centered around the Lagrangian volume of the halo of interest. The nested grids that contain finer grids have 8 cells between its boundary and its child grid. The finest grid has an equivalent resolution of a 1024^3 unigrid and a side length of 250 (300) comoving kpc. This resolution results in a DM particle mass of 30 (101) M_{\odot} and an initial gas resolution of 6.2 (21) M_{\odot} . These simula-

tions continue from the endpoints of simulations A6 and B6 of Paper I. Table 2 lists the parameters of the most massive halo in each realization. We evolve the system until the central object has collapsed and reached our resolution limit. There are 1.23×10^8 (498³) and 7.40×10^7 (420³) unique cells in the final simulation output of simulations A and B, respectively. The finest grid then has a refinement level of 41 and a spatial resolution of roughly 0.01 of a solar radius in both simulations.

Enzo employs a non-equilibrium chemistry model (Abel et al. 1997; Anninos et al. 1997), and we consider six species in a primordial gas (H, H⁺, He, He⁺, He⁺⁺, e⁻). Compton cooling and heating of free electrons from the CMB and radiative losses from atomic cooling are computed in the optically thin limit. At high densities in the halo cores, the baryonic component dominates the material. However, the discrete sampling of the DM potential by particles can become inadequate, and artificial heating (cooling) of the baryons (DM) can occur. To combat this effect, we smooth the DM particles in cells with a width < 0.24 (< 0.36) comoving pc, which corresponds to a refinement level of 15.

3. RESULTS

In this section, we first describe how the halo collapses when it starts to cool through Ly α line emission. Then we discuss the role of turbulence in the collapse. Last we describe the rotational properties and stability of the halo and central object.

3.1. Halo Collapse

Beginning at $z = 21.1$ in simulation A, the progenitor of the final halo ($M_{\text{vir}} = 4.96 \times 10^6 M_{\odot}$) starts to experience two major mergers, which continues until $z = 17.2$ when $M_{\text{vir}} = 2.36 \times 10^7 M_{\odot}$. We define M_{vir} as the mass M_{200} in a sphere that encloses an average DM overdensity of 200. In simulation B, no recent major merger occurs before the cooling gas starts to collapse, but it

⁴ To simplify the discussion, simulation A will always be quoted first with the value from simulation B in parentheses.

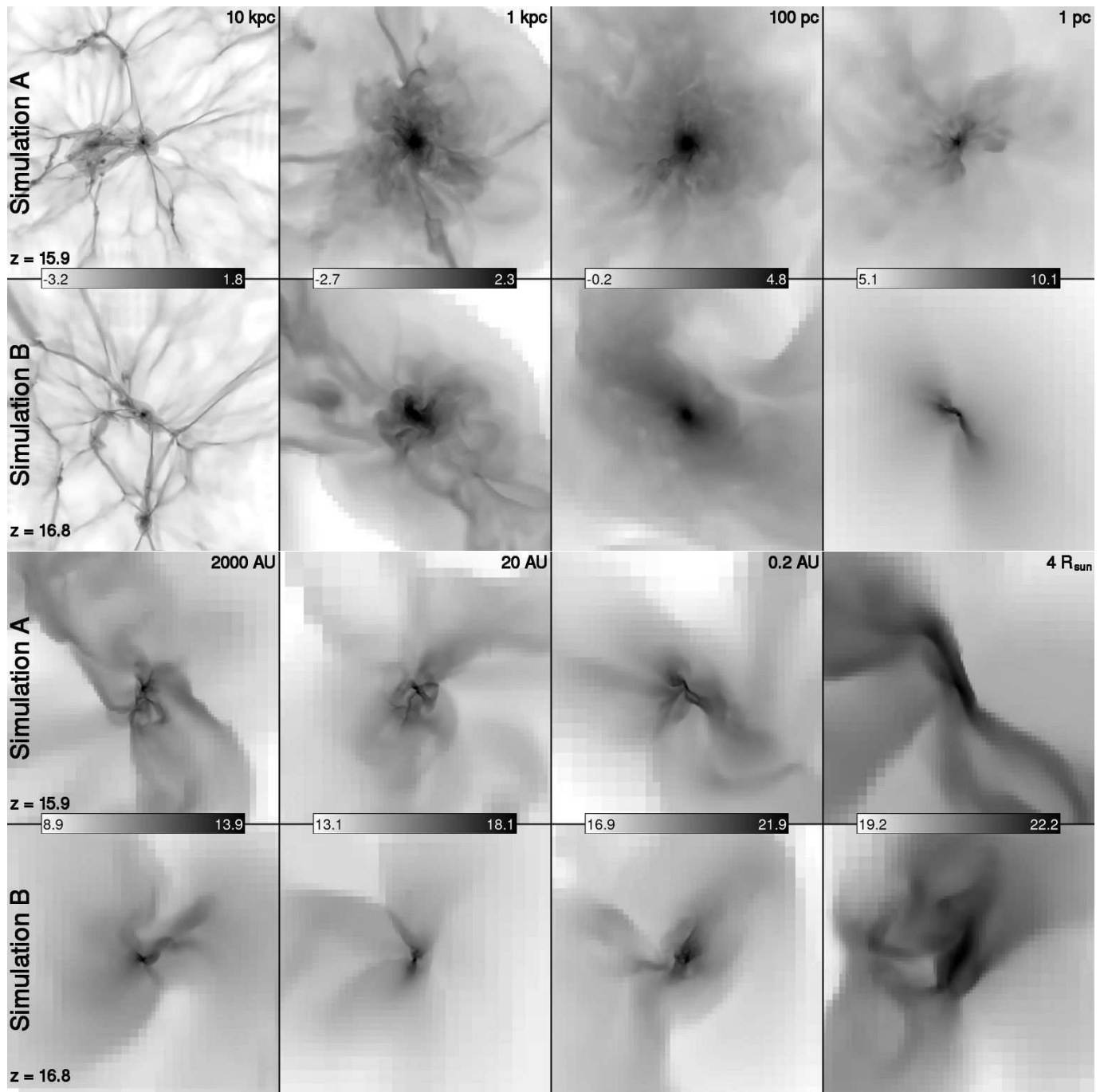


FIG. 1.— An overview of the final state of the collapsing protogalactic gas cloud. Slices of log gas density in cm^{-3} are shown through the densest point in the halo. The *first* and *third* rows show simulation A, and the *second* and *fourth* rows show simulation B. The columns in the top two rows from left to right are slices with a field of view of 10 kpc, 1 kpc, 100 pc, and 1 pc. For the bottom two rows, the fields of view are 0.01pc, 20AU, 0.2AU, and $4 R_{\odot}$. Note that each color scale is logarithmic, spans 5 orders of magnitude, and is unique for every length scale.

accumulates mass by accretion and minor mergers.

Mergers disrupt the relaxed state of the progenitor and create turbulence as these systems collide and combine. Additional turbulence arises during virialization, as discussed in Paper I. More small scale density fluctuations are thus present in simulation A. These fluctuations penetrate farther into the potential well in simulation A to scales⁵ of 1 pc, compared to simulation B that contains

⁵ Note that all masses concerning the collapse are gas mass, not total mass. The central regions of $r < 10$ pc are baryon dominated

nearly no fluctuations between 1 and 50 pc. This is apparent in the $l = 1$ pc panels of Figure 1 that show the density slices at eight length scales covering 11 orders of magnitude. At the 10 kpc scale, the filamentary large-scale structure is shown, and the protogalactic halo exists at the intersection of these filaments. In the next scale, we show the protogalactic gas cloud. At the 100 pc scale, a thick disc is seen in simulation B. It is nearly edge-on

so that $M_{\text{enc, gas}} \approx M_{\text{enc, tot}}$. All length scales are in proper units unless otherwise noted.

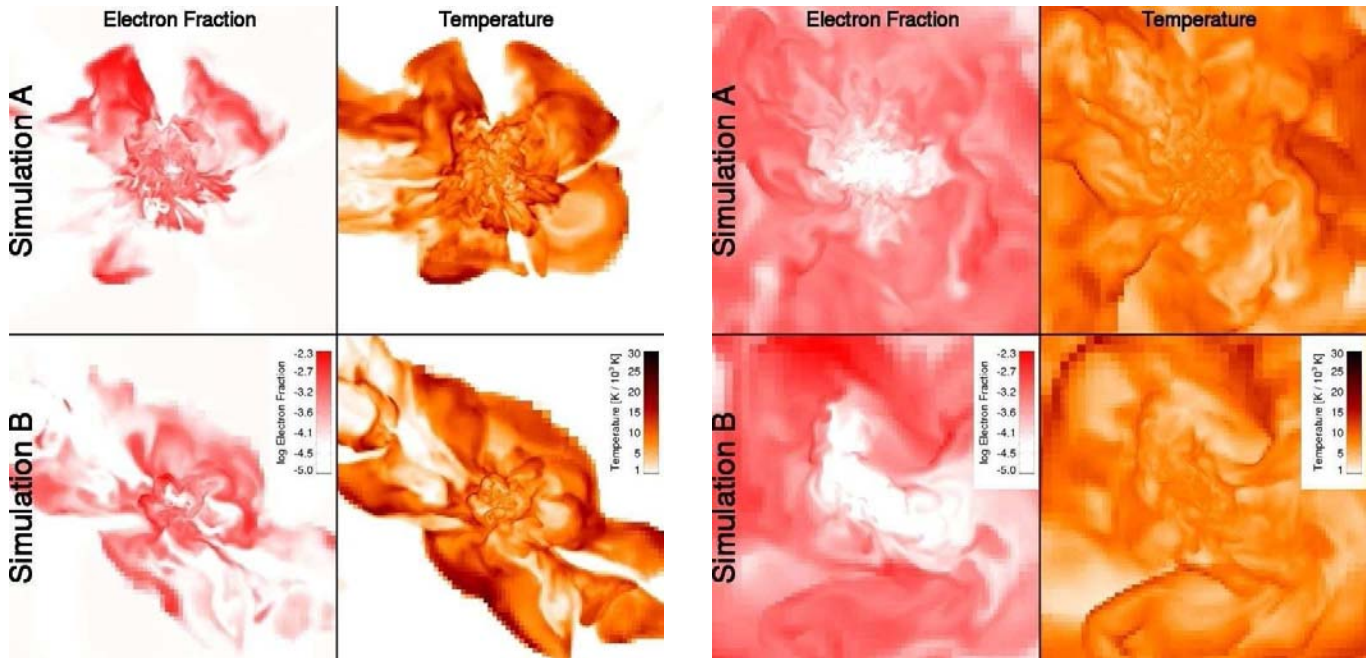


FIG. 2.— Slices of electron fraction (*left*) and temperature (*right*) of simulation A (*top*) and B (*bottom*). The field of view is 1.5 kpc (*left panels*) and 200 pc (*right panels*). The color scale is logarithmic for electron fraction and linear for temperature in units of 10^3 K. Supersonic turbulent shocks are ubiquitous throughout the halos.

and oriented northwest to southeast in this view. In simulation B at 1 pc, a bar forms from a rotational secular instability that transports angular momentum outwards. Similar instabilities exist at radii of 0.2 pc, 2700 AU, 17 AU, $0.5 R_{\odot}$ in simulation B. Simulation A also undergoes a secular bar instability at smaller scales at radii of 150 AU, 1.3 AU, $0.8 R_{\odot}$ but shows a more disorganized medium at larger scales.

The virial temperatures are now $\geq 10^4$ K, and therefore they can efficiently cool by atomic hydrogen transitions. The gas fulfills the critical condition for contraction, $t_{\text{dyn}} > t_{\text{cool}}$, and proceeds to continuously collapse in approximately a dynamical time. Figure 2 depicts slices of electron fraction and gas temperature at scales of 200 and 1500 pc. At the larger scale, the gas is heated both in virial shocks at $r \sim 600$ pc and internal turbulent shocks. Gas within the virial radius varies between ~ 2000 K in cold inflows from filaments and up to 30,000 K in turbulent shocks. Electron fractions increase to up to 0.5% because of collisional ionizations behind the shocks. The majority of the ionizations occur in the turbulent shocks inside r_{vir} where the densities are greater and temperatures at the shocks are similar to values in the virial shock. In the inner 200 pc, turbulent shocks are widespread as seen in the temperature variations. However these are less pronounced than the ones at larger radius. In the central 50 pc, the gas becomes nearly isothermal despite the low free electron fraction.

The halo collapses in two stages. We denote the beginning of the first stage when $t_{\text{dyn}} > t_{\text{cool}}$ for the first time. The second stage begins when the central object becomes gravitationally unstable.

1. *Cooling stage*— As mass infalls toward the center, the increased cooling rate, which is $\propto nn_e$, catalyzes the collapse as atomic line transitions convert kinetic energy to radiation. Here n and n_e are the number density of baryons and electrons, respectively. The first stage starts

520 (40) kyr before the last output. The inner 100 pc have a steady decrease in electron fraction that indicates atomic hydrogen cooling is now efficient in this region, which can be seen in the 200 pc slices of Figure 2. However, only the gas within 1.5 (1.0) pc has $t_{\text{dyn}} \gtrsim t_{\text{cool}} = 383$ (100) kyr at this epoch.

2. *Gravitationally unstable stage*— This starts when the central region becomes unstable to gravitational collapse. Ebert (1955) and Bonnor (1955) investigated the stability of an isothermal sphere with an external pressure P_{ext} and discovered that the critical mass (BE mass hereafter) for gravitational collapse is

$$M_{\text{BE}} = 1.18 \frac{c_s^4}{G^{3/2} P_{\text{ext}}^{1/2}} M_{\odot}. \quad (1)$$

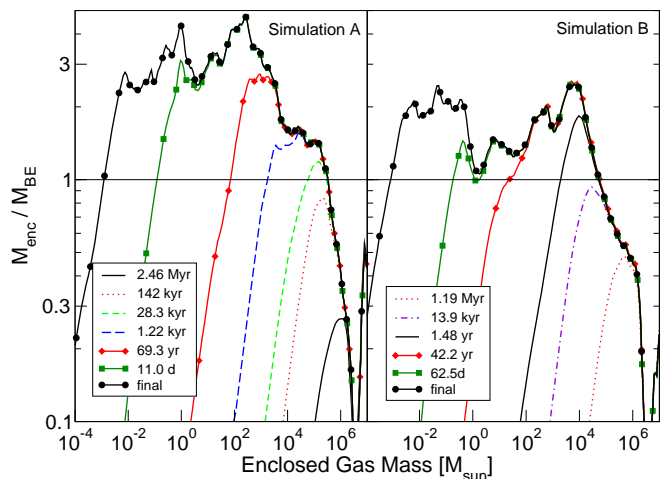


FIG. 3.— The ratio of the enclosed gas mass and Bonnor-Ebert mass (eq. 1) for the final output (*black with circles*) and selected previous times that are listed in the legend. Simulation A (*left*) and B (*right*). For values above the horizontal line at $M_{\text{enc}}/M_{\text{BE}} = 1$, the system is gravitationally unstable.

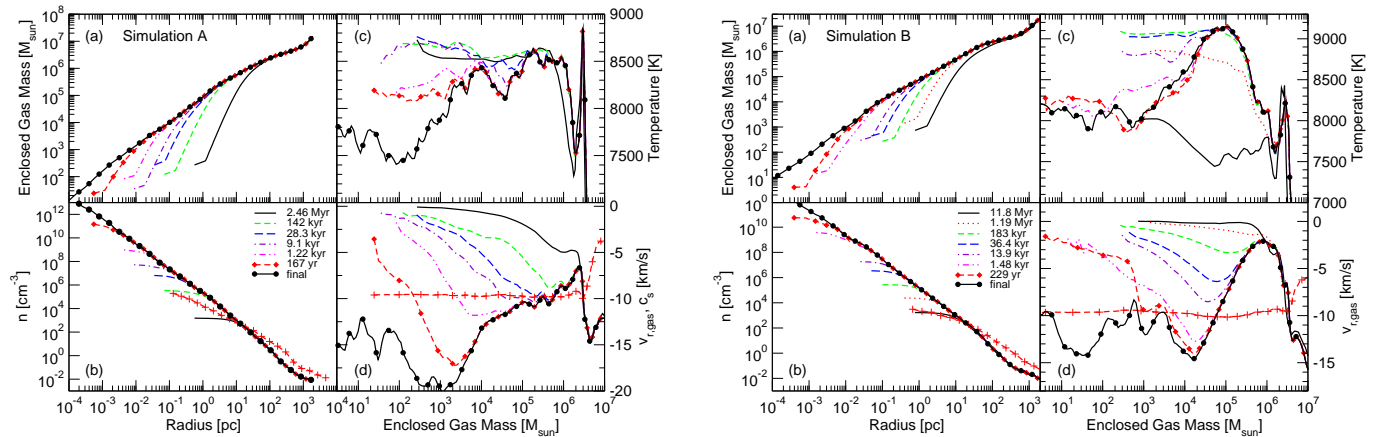


FIG. 4.— Mass-weighted radial profiles at various times of (a) gas mass enclosed, (b) number density, (c) mass-weighted temperature, and (d) mass-weighted radial velocity for simulation A (*left panels*) and simulation B (*right panels*). The quantities in the left and right panels are plotted with respect to radius and gas mass enclosed, respectively. In (b), the dashed line with crosses is the dark matter density in units of $m_H \text{ cm}^{-3}$. In (d), the dashed line with crosses is the negative of the sound speed in the final output. The times in the legends correspond to time before the end of the simulation.

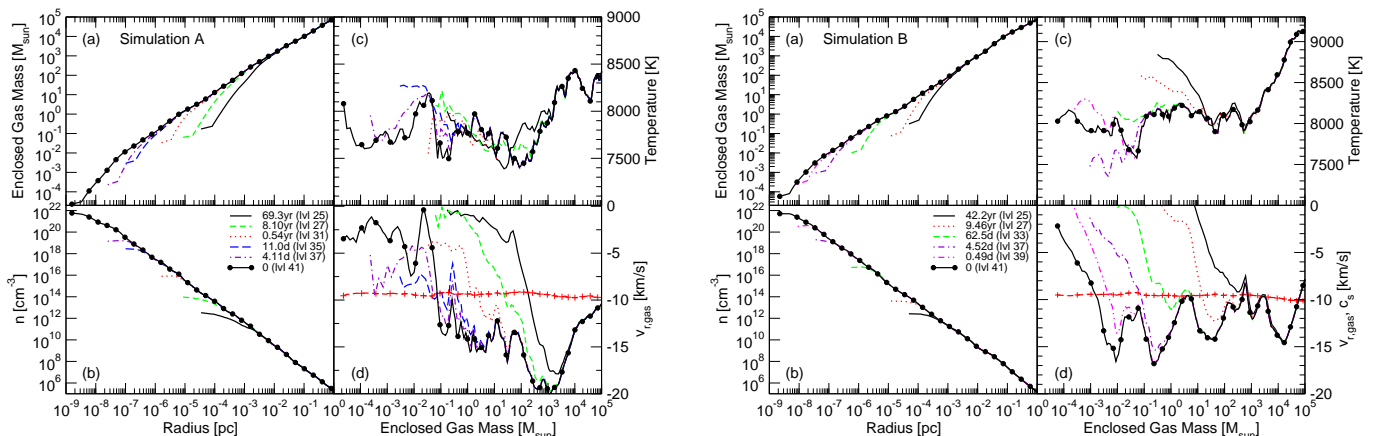


FIG. 5.— Same as Figure 4 for the inner parsec of simulation A (*left panels*) and simulation B (*right panels*). The maximum AMR level is listed next to the times in the legend. In simulation B, the local minima in radial velocities at 2×10^4 , 40, 0.3, and $0.01 M_\odot$ occur as angular momentum is transported outwards in secular bar-like instabilities.

If we set P_{ext} to the local pressure, then

$$M_{BE} \approx 20T^{3/2}n^{-1/2}\mu^{-2}\gamma^2M_\odot. \quad (2)$$

For both simulations, this stage occurs between 10 and 100 kyr before we end the simulation. We plot the ratio of the enclosed gas mass and BE mass in Figure 3 for several epochs in the collapse. When the clump becomes gravitationally unstable, the central 3.3×10^5 (5.5×10^4) M_\odot in the central $r_{BE} = 5.8$ (0.9) pc exceeds the BE mass, and its $t_{dyn} = 520$ (80) kyr. Thus our numerical results agree with these analytic expectations.

We follow the evolution of the accretion and contraction until the simulation⁶ reaches a refinement level of 41 (41) that corresponds to a resolution of 0.01 (0.014) R_\odot . At this point, the central 4.7×10^5 (1.0×10^5) M_\odot are gravitationally unstable and *not* rotationally supported. The central mass is nearly devoid of free electrons where the electron fraction, $n_e/n < 10^{-6}$, and the temperature is ~ 8000 K. It has a radius of 7.9 (1.5) pc. The central number density is 5.8 (7.6) $\times 10^{21} \text{ cm}^{-3}$.

⁶ We stop the simulation because of ensuing round-off errors from a lack of precision. We use 80-bit precision arithmetic for positions and time throughout the calculation.

Next we show the radial profiles of the final and preceding outputs in Figures 4 and 5, where we plot (a) enclosed gas mass, (b) number density, (c) mass-weighted temperature, and (d) mass-weighted radial velocity. Figure 4 focuses on length scales greater than 20 AU to $r > r_{vir}$. The halo collapses in a self-similar manner with $\rho(r) \propto r^{-12/5}$. We also overplot the DM density in units of $m_H \text{ cm}^{-3}$ in the *b* panels. The DM density in simulation A does not flatten as much as simulation B with $\rho_{DM} \propto r^{-4/3}$ and $r^{-2/3}$, respectively, yet higher DM resolution simulations will be needed to address the significance of this difference in central slopes. In the *c* panels, one sees that the entire system is isothermal within 10% of 8000 K. In the *d* panels, the sound speed c_s in the final epoch is plotted, and there is a shock where $v_r > c_s$ at a mass scale when M_{enc} first exceeded M_{BE} . Here v_r is the radial velocity, and c_s is the local sound speed.

Figure 5 shows the data within 1 pc at times 100 years before the end of the simulation. The self-similar, isothermal collapse continues to stellar scales. However, the structure in the radial velocity in simulation B exhibits a strikingly behavior with four repeated minima at mass scales 2×10^4 , 10^3 , 6, and $10^{-3} M_\odot$. We attribute

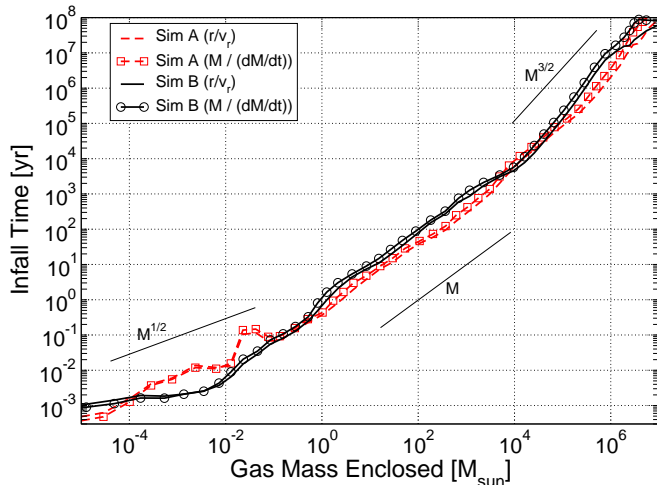


FIG. 6.— Radial profiles of gas infall times at the final output. To approximate a collapse timescale, the quantities r/v_r (solid) and $M/(dM/dt)$ (dashed) are calculated and plotted here.

this to rotational bar-like instabilities that we discuss later in the paper (§3.6).

If we consider v_r constant from the last output, we can determine the infall times, which are shown in Figure 6. The infall time, $t_{in} = r/v_r$, of the shocked BE mass is 350 (50) kyr. The infall times approximately follow a broken power law, $t_{in} \propto M_{enc}^\beta$. Within $M_{enc} \sim 0.1M_\odot$, $\beta \approx 1/2$. In the range $0.1 \lesssim M_{enc}/M_\odot \lesssim 3 \times 10^4$, $\beta \approx 1$; above this mass interval, the slope of the mass infall times increase to $\beta \approx 3/2$. The increased radial velocities when the central object becomes gravitationally unstable causes the steepening of the slope at $\sim 3 \times 10^4 M_\odot$.

3.2. Global Disc

In simulation B, a thick disc with a radius of 50 pc and disc scale height of ~ 10 pc forms that is pressure supported and only partially rotationally supported. The circular velocities within this disc achieve only a third of Keplerian velocities. The lack of full rotational support and large scale height suggests that a central collapse occurs before any fragmentation in this large-scale disc is possible. In contrast, we see a disorganized, turbulent medium and no large scale disc formation in simulation A.

3.3. Turbulence

Kolmogorov (1941) described a theory of the basic behavior of incompressible turbulence that is driven on a large scale and forms eddies at that scale. These eddies then interact to form smaller eddies and transfer some of their energy to smaller scales. This cascade continues until energy is dissipated through viscosity. In supersonic turbulence, most of the turbulent energy is dissipated through shock waves, which minimizes the local nature of cascades found in incompressible turbulence.

In Paper I, we found that turbulence is stirred during virialization. When radiative cooling is efficient, the gas cannot virialize by gaining thermal energy and must increase its kinetic energy in order to reach equilibrium, which it achieves by radial infall and turbulent motions.

In addition to virial turbulence generation, mergers stir turbulence. Here the largest driving scale will be approximately the scale of the merging objects, and the turbu-

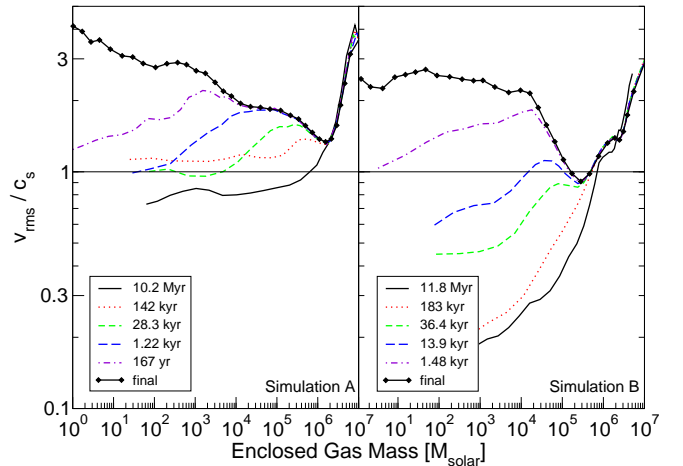


FIG. 7.— The turbulent Mach number, v_{rms}/c_s , for the final output (black with diamonds) and selected previous times that are listed in the legend. Simulation A (left) and B (right).

lent cascade starts from that length scale. Additional driving may come from Kelvin-Helmholtz instabilities of a multi-phase gas as the mergers occur (Takizawa 2005). Takizawa considered mergers of galaxy clusters, however his work may still apply to the formation of protogalactic halos since similar temperature contrasts exist in this regime of mergers. As the lesser halo falls into the massive halo, a bow shock and small-scale eddies from the Kelvin-Helmholtz instability form between the two interacting objects. At later times, a dense, cool core remains in the substructure of the lesser halo. The instabilities grow and destroy the baryonic substructure, and the gas mixes with the existing gas of the massive halo and becomes turbulent.

To quantify aspects of this turbulence, we inspect the turbulent Mach number,

$$\mathcal{M} = \frac{v_{rms}}{c_s}; \quad c_s^2 = \frac{dP}{d\rho} = \frac{\gamma kT}{\mu m_H}. \quad (3)$$

Here P is pressure, v_{rms} is the 3D velocity dispersion, and γ is the adiabatic index that we set to $5/3$. We evaluate v_{rms} with respect to the mean velocity of each spherical shell. Radial profiles of \mathcal{M} are shown in Figure 7. Before the core becomes gravitationally unstable, the turbulence is subsonic within the virial shock. After the core becomes gravitationally unstable, the turbulent Mach number rises to 2–4. The collapse produces turbulence on a timescale that is faster than it can be dissipated.

The turbulence that exists before the initial collapse may impact the nature of the central object. In simulation A, the core initially has $\mathcal{M} \approx 1$, and this results in a central object with $4.7 \times 10^5 M_\odot$ and a radius of 7.9 pc. The core in simulation B has $\mathcal{M} \approx 0.2$, and the central object is about five times less massive and smaller, which corresponds to a free-fall time approximately five times shorter as well.

3.4. Spin Parameter Evolution

During the hierarchical buildup of structure, tidal forces from neighboring structures impart angular momentum to a halo, particularly when its radius is maximal at the turn-around time (Hoyle 1949; Peebles 1969).

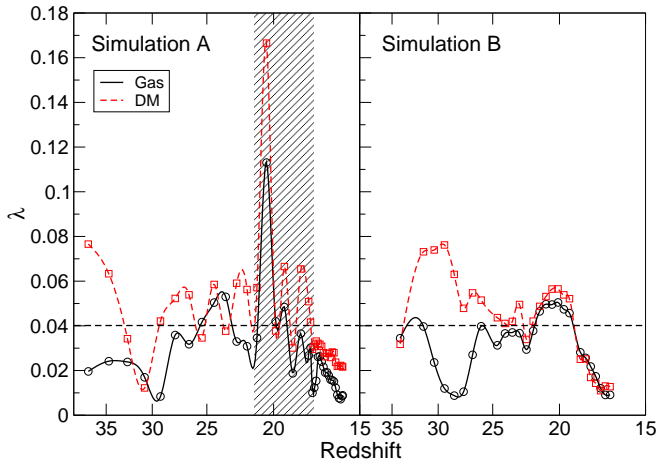


FIG. 8.— Spin parameter, $\lambda \equiv |L|\sqrt{|E|}/GM^{5/2}$, evolution of the main halo in the simulation. (*left*) simulation A. (*right*) simulation B. The dashed and solid lines are the interpolated values for the DM and baryonic spin parameter. The squares and circles correspond to the actual measurements from the DM and gas data, respectively. The horizontal dashed line at $\lambda = 0.04$ marks the mean cosmological spin parameter. In simulation A, two major mergers causes the large increase beginning at $z \approx 21$ in the hashed region. The oscillations occur as the merging halos orbit each other until they virialize.

However in recent years, several groups have recognized that the mergers may impart a considerable fraction of angular momentum to the system (Steinmetz & Bartelmann 1995; Gardner 2001; Vitvitska et al. 2002; Maller et al. 2002). Over many realizations of mergers, the net angular momentum change would be zero. In reality, an angular momentum residual remains after the last major merger occurs because there are too few events to cancel the randomization of halo spin. Although each halo has unique rotational properties, it is useful to define a dimensionless spin parameter

$$\lambda \equiv \frac{|L|\sqrt{|E|}}{GM^{5/2}}, \quad (4)$$

where G is the gravitational constant and L , E , and M are the angular momentum, energy, and mass of the object, that measures the rigid body rotation of the halo (Peebles 1971). In Figure 8, we display the time evolution of λ of the DM and baryons in our simulations and mark the occurrence of the major merger in simulation A. Eisenstein & Loeb (1995b) (preceded by Barnes & Efstathiou 1987) calculated that the mean spin parameter, $\langle \lambda \rangle \approx 0.04$, is weakly dependent on object mass and cosmological model, and this value is also marked in Figure 8. Also λ weakly depends on its merger history, where $\langle \lambda \rangle$ increases during mergers and slowly dissipates afterwards. Most of the angular momentum is acquired from steady minor mergers and accretion because major mergers only happen rarely (usually only once per logarithmic mass interval). In 96% of mergers, the majority of the internal spin originates from the orbital energy of the infalling halo (Hetznecker & Burkert 2006).

At $z \approx 22$ in simulation A, the spin parameter $\lambda = 0.06$ before the last major merger. Then the spin parameter increases by a factor of 3 during its major merger because of the system being far from dynamical equilibrium. The system becomes virialized after approximately a dynamical time, and the spin parameter stabilizes at $\lambda \approx 0.03$ and proceeds to decrease with time until $\lambda = 0.022$ at

the time of collapse. The above evolution of λ agrees with the findings of Hetznecker & Burkert. Simulation B describes a halo that does not undergo a recent major merger, and its final $\lambda = 0.013$.

Both halos have less angular momentum than $\langle \lambda \rangle$ when the cooling gas collapses. The probability distribution of λ can be described with the log-normal function

$$p(\lambda)d\lambda = \frac{1}{\sigma_\lambda\sqrt{2\pi}} \exp\left[-\frac{\ln^2(\lambda/\lambda_0)}{2\sigma_\lambda^2}\right] \frac{d\lambda}{\lambda}, \quad (5)$$

where $\lambda_0 = 0.042 \pm 0.006$ and $\sigma_\lambda = 0.5 \pm 0.04$ (e.g. Bullock et al. 2001). From the cumulative probability function resulting from equation (5), 89% (99%) of the cosmological sample of halos have larger spin parameters than the halos described here. Eisenstein & Loeb (1995a) demonstrated that halos with low spin parameters are candidates for BH formation and quasar seeds. However they argue that the angular momentum needs to be at least an order of magnitude lower than the mean. Next we present further evidence that reveals a gaseous collapse is possible with not too atypical spin parameters.

3.5. Instability of Maclaurin Spheroids

The dynamics of rotating systems is a classic topic in astrophysics (see EFE §§1–6). These self-gravitating systems are susceptible to two types of instabilities. Secular instability occurs when small dissipative forces, e.g. viscosity, amplify perturbations to become unstable in an otherwise stable inviscid configuration. Dynamical (also referred to as ordinary) instability results when some oscillatory mode exponentially grows with time, regardless of any dissipative forces. Here we concentrate on Maclaurin spheroids relevant for a uniform body rotating with a fixed angular velocity. Maclaurin spheroids are a special case of Jacobi ellipsoids that are axisymmetric. The onset of the $m = 2$ bar-like instability in gaseous Maclaurin spheroids happens for a given eccentricity,

$$e = \left(1 - \frac{a_3^2}{a_1^2}\right)^{1/2} \geq \begin{cases} 0.8127 & \text{(secular)} \\ 0.9527 & \text{(dynamical)} \end{cases}, \quad (6)$$

where a_3 and a_1 are the principle axes with $a_3 \leq a_1$ (EFE §33). Eccentricity is related to the ratio, $t = T/|W|$, of rotational kinetic energy to gravitational potential by

$$t = \frac{1}{2}[(3e^{-2} - 2) - 3(e^{-2} - 1)^{1/2}(\sin^{-1} e)^{-1}], \quad (7)$$

and the secular and dynamical instabilities happen at $t = (0.1375, 0.27)$, respectively (e.g. Ostriker & Peebles 1973).

When t is larger than 0.1375 but smaller than 0.27, both the Maclaurin spheroid and Jacobi ellipsoid are perfectly stable against small perturbations in the inviscid case. For a given e , the Jacobi configuration has a lower total energy than its Maclaurin counterpart and is therefore a preferred state. Here any dissipative force induces a secular bar-like instability. The system slowly and monotonically deforms through a series of Riemann S-type ellipsoids until its final state of a Jacobi ellipsoid with an equal angular momentum (Press & Teukolsky 1973) and lower angular velocity (EFE §32) as specific angular momentum is transported outward. The instability grows on an e -folding timescale

$$\tau = \phi a_1^2/\nu, \quad (8)$$

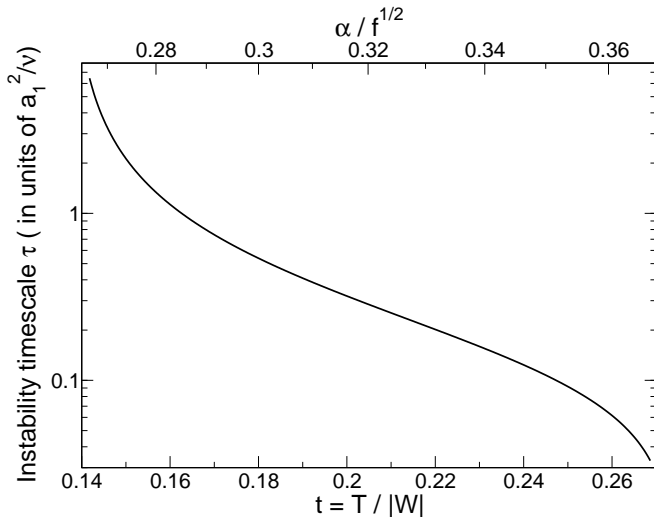


FIG. 9.— Secular instability e -folding timescale in units of a_1^2/ν as a function of $t = T/|W|$ and $\alpha = (tf/2)^{1/2}$ (eq. 9). At $t < 0.1375$, the system is stable to all perturbations. Above $t = 0.27$, the system is dynamically unstable, and this timescale is not applicable.

where ϕ is a constant of proportionality that asymptotes at $t = 0.1375$, decays to zero at $t = 0.27$, and is plotted in Figure 9 (EFE §37). Here ν is the kinematic viscosity.

Christodoulou et al. (1995a,b) generalized the formulations for bar-like instabilities to account for self-gravity. In addition, they consider different geometries, differential rotation, and non-uniform density distributions. They devised a new stability criterion

$$\alpha \equiv \frac{T/|W|}{\Omega/\Omega_J} = \sqrt{\frac{f}{2} \frac{T}{|W|}} \quad (9)$$

where Ω is the rotation frequency,

$$\Omega_J^2 = 2\pi G\rho \left[\frac{(1-e^2)^{1/2}}{e^3} \sin^{-1} e - \frac{1-e^2}{e^2} \right] \quad (10)$$

is the Jeans frequency in the radial direction for a Maclaurin spheroid, and

$$f = \frac{1}{e^2} \left[1 - \frac{e}{\sin^{-1} e} \sqrt{1-e^2} \right] \quad (11)$$

accounts for differing geometries⁷ with $f = 2/3$ for a sphere and $f = 1$ for a disc. Secular and dynamical instabilities for Maclaurin spheroids occur above $\alpha = (0.228, 0.341)$, respectively, for $f = 1$.

From N-body simulations of disc galaxies, Ostriker & Peebles (1973) found that a massive dark halo with comparable mass to the disc could suppress secular instabilities. In the case of a gaseous collapse to a SMBH however, the baryonic component dominates over the dark matter component in the central 10 pc. Secular instabilities cannot be prevented through this process, which we demonstrate next.

3.6. Rotational Instabilities

In the $l = 1$ pc panel of simulation B in Figure 1, it is apparent a bar-like instability exists in the gravitationally unstable central object. Figure 10 shows the instability criterion α (eq. 9) against enclosed gas mass. Here

⁷ See Christodoulou et al. (1995b) for more generalized geometries.

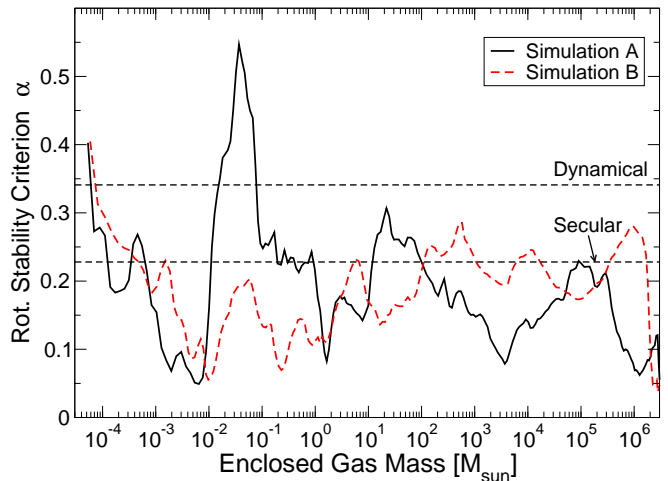


FIG. 10.— Rotational instability parameter $\alpha = \sqrt{fT/2|W|}$ for the thick disc with $r \simeq 50$ pc in simulations A (black solid line) and B (red dashed line). For $\alpha > 0.22$ denoted by the horizontal line, a secular instability occurs in the disc and leads to bar formation. In simulation A, instabilities occur at mass scales of 100, 0.1, and $10^{-4} M_\odot$. In simulation B, the same happens at 2×10^6 , 2×10^4 , 10^3 , 6, and $10^{-3} M_\odot$. We also mark $\alpha = 0.341$ where a rotating system becomes dynamically unstable. Only simulation A at $0.1 M_\odot$ experiences a dynamical instability.

we transform the velocities to align the z -axis with the baryonic angular momentum vector of the entire halo. We use the tangential velocities to calculate the rotational kinetic energy T . The shape parameter $f = 2/3$ (0.89) for simulation A (B).

As discussed before, Maclaurin spheroids are subject to secular $m = 2$ bar-like instabilities when $\alpha > 0.228$. In simulation A, the central object becomes unstable three approximate mass scales, 6.7×10^{-4} , 1.0, and $110 M_\odot$ that correspond to radii of $0.75 R_\odot$, 1.3 AU, and 150 AU, respectively. The enclosed mass ratios of the recurring instabilities, i.e. M_i/M_{i+1} , are 1500:1, 110:1, and 1400:1, starting at the smallest mass scale. The instability at $0.075 M_\odot$ ($r = 0.13$ AU) is dynamically unstable with α peaking at 0.55. In simulation B, instabilities occur at 5.3×10^{-4} , 7.0, 1.2×10^3 , and $2.0 \times 10^4 M_\odot$ at radii of 0.49 R_\odot , 17 AU, 2700 AU, and 0.18 pc. The enclosed mass ratios of these instabilities, are 13,000:1, 170:1, 17:1, and 85:1.

It is interesting to note that the innermost instability in both simulations becomes dynamical ($\alpha > 0.341$), and α continues to increase rapidly toward the center. However these features should be taken with caution since it occurs near our resolution limit, where the particular location used as the center will influence the rotational energy one would calculate.

The e -folding time of secular instabilities τ is proportional to a_1^2 (see eq. 8). Hence small-scale instabilities collapse on a faster timescale than its parent, large-scale bar instability. Turbulent viscosity is the main dissipative force that drives the instability. τ is inversely proportional to the viscosity. This further shortens τ because supersonic turbulence is maintained to the smallest scales.

3.7. Rotational Properties

During the collapse of the gas in our simulations, rotational support never impedes the collapse. In Figures

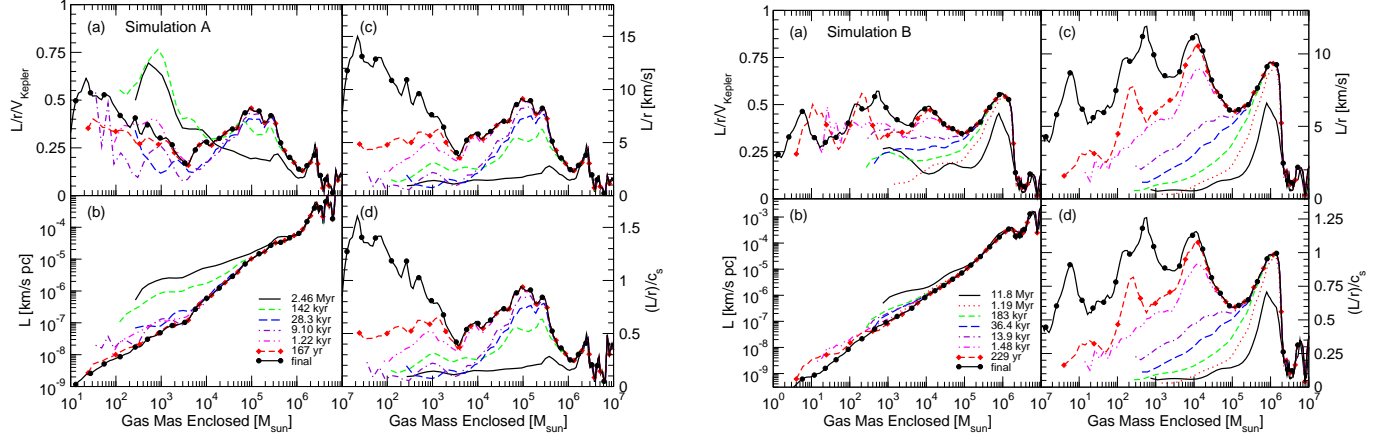


FIG. 11.— Mass-weighted radial profiles of various rotational quantities in simulation A (left panels) and simulation B (right panels). In panel A, we show the rotational velocity compared to the Kepler velocity $= \sqrt{GM/r}$. In panel B, we display the typical rotational velocity. In panels C and D, the specific angular momentum (in units of km/s pc) and the ratio of the rotational velocity and sound speed is shown, respectively. The line styles correspond to the same times in Figure 4.

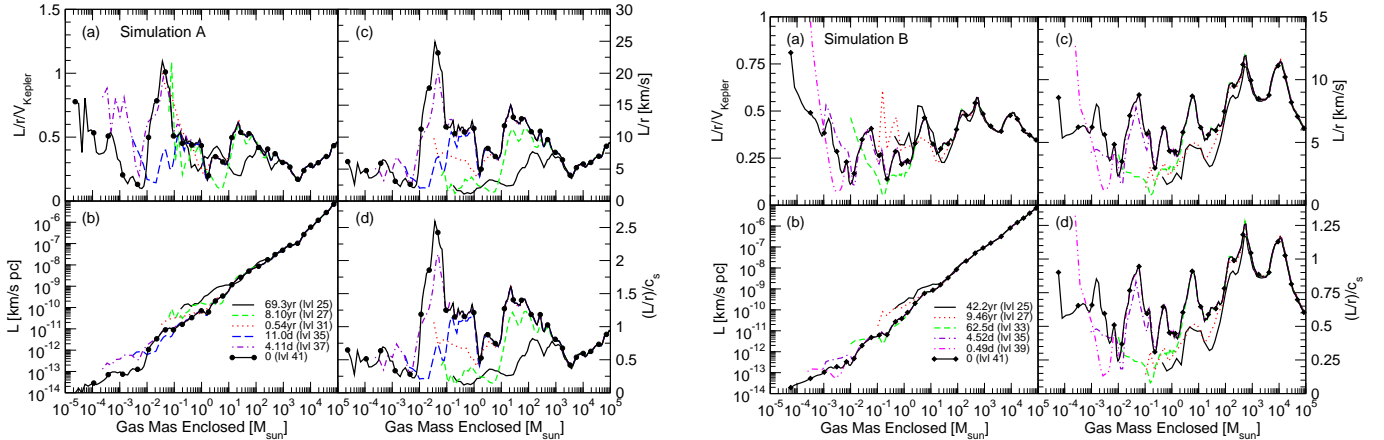


FIG. 12.— The same as Figure 11 but with the inner parsec of simulation A and B and the output times as listed in Figure 5.

11 and 12, we show (a) coherent rotational velocity divided by Keplerian velocity $v_{kep} = \sqrt{GM/r}$, (b) rotational velocity, (c) specific angular momentum, and (d) rotational velocity divided by the sound speed. We compute the rotational velocities around the center of mass of a sphere with radius of 100 cell widths of the finest AMR level, centered on the densest point. We note that the rotational velocity L/r plotted here is different than organized rotation, i.e. a disc. The radial profiles only sample gas in spherical shells, whose angular momentum vectors are not necessarily parallel.

1. *Simulation A*— At $r > 1$ AU ($M_{enc} = 1M_{\odot}$), the typical rotational speed is two or three times lower than the Keplerian velocity, which is required for rotational support. At $r = 0.1$ AU ($M_{enc} = 0.07 M_{\odot}$), the infall becomes marginally rotationally supported, i.e. $L/r \sim v_{kep}$. The radial velocities react by slowing from 15 km s $^{-1}$ to below 5 km s $^{-1}$. However this rotational support does not continue to the center. Rotational speeds are only $\sim 0.5v_{kep}$ within 0.1 AU ($M_{enc} = 1M_{\odot}$).

2. *Simulation B*— This collapse exhibits four minima in radial velocity that are caused by rotational bar-like instabilities. After such an instability occurs, the radial velocities increase because of angular momentum being transported outwards. As the rotational veloci-

ties decrease, this instigates another secular instability, which repeats causing a cascade of the instability. The increased infall velocity and associated decrease in rotational velocities (i.e. the dips in Figures 5d and 12d) depict this behavior. At the final output, the infalling material exhibits no rotational support at all radii similar to simulation A at $r > 1$ AU.

We interpret the inner points where $L/r/v_{kep}$ fluctuations greatly or increases above unity with caution because of the nature of choosing a center in a turbulent medium, i.e. when turbulent velocities dominate over rotational ones. If the central sphere is smaller than a radius where the turbulent velocities average to zero, we introduce errors into the angular momentum profiles by sampling the turbulent gas incompletely. In the *b*-panels of Figure 11, one sees that specific angular momentum inside $M_{enc} < 10^6 M_{\odot}$ decreases over time and is transported outwards in the collapse.

With a not too atypical spin parameter, the thick disc with $r \sim 50$ pc is not rotationally supported. In simulation A, a global disc does not exist at all. We attribute this behavior to the nature of angular momentum transport in a turbulent medium. Even with a higher spin parameter, we do not expect a disc to fragment before the central collapse of small amounts of low angular momen-

tum gas and shorter dynamical timescales in the center. This low specific angular momentum material collapses to small radii without fragmentation so that a central dense object forms with a mass of $\sim 10^5 M_\odot$ or 2% of the halo gas mass. After the initial collapse, the thick disc may become rotationally supported as more high angular momentum gas infalls.

4. DISCUSSION

In our cosmological simulations, we find that a $\sim 10^5 M_\odot$ dense object forms in the center of a metal-free protogalactic halo that cools by atomic hydrogen cooling. Although we have neglected some important processes, such as H_2 chemistry, star and BH formation and feedback, our results show that angular momentum transport at both small and large scales in the form of preferential segregation and rotational instabilities, respectively, lead to the formation of a dense, massive object with $r < 5$ pc. This initial central collapse should precede any fragmentation of a global disc.

4.1. Angular Momentum Transport

Collapsing turbulent clouds, whether cosmological or galactic in nature, are ubiquitous in the universe. In this paper, we focus on the details of the turbulent collapse of a proto-galactic halo. Angular momentum transport plays a key role in such events, e.g., determining the characteristics of the central object(s). However there exists the “angular momentum problem”, where many orders of magnitude of angular momentum must be shed (see §6 in Larson 2003) from the initial molecular cloud to form a central star, star cluster, or BH. In our simulations, there is a clear scenario in which the inside-out collapse (Shu et al. 1987) proceeds even if the initial turbulent cloud was rotating. We see three major elements affecting angular momentum transport during the collapse.

1. *Angular momentum distribution*— In cosmological halos, there is a universal distribution of angular momentum

$$M(< j) = M_{\text{vir}} \frac{\mu j}{j_0 + j}, \quad \mu > 1, \quad (12)$$

that measures the mass with a specific angular momentum less than j (Bullock et al. 2001). This function is fitted with two parameters, μ and j_0 , where μ controls the flattening of the power law at high angular momenta, and j_0 determines at which j this transition occurs. Bullock et al. also find that more mass resides in the tails of the distribution, especially at small j , when compared to a system in solid body rotation. Thus all halos have some intrinsic amount of gas with small j . If this distribution is maintained during the collapse (e.g. Messtel 1963), such gas can collapse to some small radius, $r_{\text{min}} > j/v_{\text{kep}}$, without becoming rotationally supported, which leads to the next element of discussion – angular momentum segregation.

2. *Segregation in a turbulent medium*— In Paper I, we determined that most of the gas becomes supersonically turbulent as a result of virialization. Therefore let us theorize how angular momentum transport happens during the transition from being pressure supported to rapidly cooling and collapsing. First consider a turbulent uniform-density gas cloud, where parcels of gas

at a specific radius can have many different values of j . This differs from the organized rotation of a disc. If we start with such an initial configuration, how does angular momentum transport occur during the collapse? Gas with small (high) j will preferentially migrate to small (large) radii, following turbulent flow lines. In an axisymmetric system, the Rayleigh criterion (Rayleigh 1920; Chandrasekhar 1961) requires that the specific angular momentum must be a monotonically increasing function with respect to radius. The gas with the lowest j progressively piles up in the center of DM potential wells until $t_{\text{cool}} > t_{\text{dyn}}$ when it can catastrophically cool and collapse. Such low j gas may originate in lower mass progenitors because the gas resided in shallow potential wells (i.e. low mass halos) that led to smaller turbulent and thermal velocities. We argue that this effect is intimately linked to the gas acting to achieve virial equilibrium at all stages during the collapse (see Paper I). Furthermore, the system becomes unstable to turbulence as the material segregates. This onset of turbulence can be delayed if viscosity is large enough so that Reynolds numbers are below the order of 10^2 or 10^3 . However there are many modes of instability if the Rayleigh criterion is not met, and even gas with a low Reynolds number will eventually become fully turbulent (Shu 1992). We note that a more comprehensive approach would consider the Solberg-Høiland criterion (Endal & Sofia 1978) that generalizes this to include partial rotational and pressure support in a disc.

3. *Bar-like rotational instabilities*— After sufficient amounts of gas have migrated to small radii because of angular momentum segregation, this gas increases its rotational velocity as it conserves angular momentum. Gas with similar angular momentum now obtains some organized rotational velocity. As the rotational energy increases, some shells may become rotationally unstable ($T/|W| \geq 0.14$) in a secular $m = 2$ mode. In the case of a collapsing gas cloud, turbulent viscosity provides the dissipative force that drives the secular instability. The system then deforms into a bar-like object, where the gas with large j moves to larger radius and gas with small j can infall to even smaller radii.

The combination of these three processes alleviates the “angular momentum problem” of inside-out collapses. Such a scenario of angular momentum transport during a self-similar collapse may be widely applicable in both cosmological collapse problems and present-day star formation problems.

4.2. Secular Instability Cascade

Our simulations follow the self-similar collapse of protogalactic halos over 14 orders of magnitude in length. We find that a cascade of three (four) bar-like instabilities occur during the latter stages of the collapse. The ratios of mass enclosed in each successive instability varies from 10 to 10,000 in our simulations. As a consequence of these instabilities, the collapse of the densest point never halts because of rotational support. Instead the gas becomes rotationally unstable when it gains sufficient rotational energy. The lowest j gas then falls to smaller radius and may become unstable yet again. This sequence could repeat itself several times. In addition, we find that rotational instabilities are possible without

a global disc as in simulation A.

This is the “bars within bars” scenario originally proposed to fuel active galactic nuclei through dynamical rotational bar-like instabilities (Shlosman et al. 1989, 1990). It was then adapted for funneling enough gas into pre-galactic ($M \sim 10^5 M_\odot$) SMBHs by Begelman et al. (2006), in whose framework the angular momentum of the disc, where the instability occurs, depends on the spin parameter of the halo (see also Mo et al. 1998). Thus the amount of gas available for accretion onto the central SMBH also depends on the spin parameter. Dynamical instabilities require 45% more rotational energy to occur than secular ones. In the framework of Begelman et al., only requiring secular instabilities may result in a larger fraction of halos forming a pre-galactic SMBH because of the log-normal distribution of spin parameters (eq. 5). Nevertheless, we do not advocate our simulations as evidence of pre-galactic SMBH formation because we have neglected many important processes related to H_2 cooling and primordial star formation that we detail briefly in the next section.

4.3. Applicability

4.3.1. Limitations of Current Approach

Our results depict the importance of turbulence, accretion, and the hydrogen cooling in the initial collapse of these halos. However we are missing some essential processes, such as H_2 chemistry, primordial and Population II stellar formation and feedback, SMBH formation and feedback, and metal transport and cooling. It was our intention to study only the hydrogen and helium cooling case first and gradually introduce other processes at a later time to investigate the magnitude and characteristics of their effects, which we will present in later papers.

Gas becomes optically thick to $Ly\alpha$ radiation above number densities of 10^7 cm^{-3} . We continue to use optically thin cooling rates above this density. Thus we overestimate the cooling within 0.1 pc. As a consequence, we do not suggest that these simulated objects ever form in nature. However this scenario poses an excellent numerical experiment of turbulent collapse, which should be common in galaxy formation, where turbulence is generated during virialization, and star formation within turbulent molecular clouds.

4.3.2. Desired Improvements

Clearly local dwarf spheroidals contain stars with ages consistent with formation at very high redshifts (Ferrara & Tolstoy 2000; Tolstoy et al. 2002, 2003; Helmi et al. 2006). To develop a model that desires to fit galaxy luminosity functions down to the faintest observed galaxies one may need a star formation and feedback model that follows molecular clouds as small as one thousand solar masses in order to allow for the dominant mode of star formation observed locally. It should be already technologically feasible with current cosmological hydrodynamical models to simulate these galaxies one star at a time.

Correct initial conditions for early galaxy formation require prior star and BH formation and feedback. The typically adopted conditions for phenomenological star formation are velocity convergence, a critical overdensity, $t_{\text{dyn}} > t_{\text{cool}}$, and being Jeans unstable (Cen & Ostriker

1992). Phenomenological primordial star formation is possible if we include two additional conditions as utilized in Abel et al. (2007). First, the H_2 fraction must exceed 10^{-3} (Abel et al. 2002), and second, the metallicity of the gas must not exceed some “critical metallicity” of $10^{-3} - 10^{-6}$ of the solar value (Bromm et al. 2001; Schneider et al. 2006; Smith & Sigurdsson 2007; Jappsen et al. 2007a,b). From prior studies (e.g. Abel et al. 2002; Bromm & Loeb 2003; O’Shea et al. 2005; Greif & Bromm 2006), we expect these stars to form to in halos that can support H_2 cooling and ones embedded in relic H II regions. The Lyman-Werner radiation from massive stars can dissociate H_2 from large distances (Dekel & Rees 1987; Haiman et al. 2000), suppress star formation in lower mass halos (Machacek et al. 2001; Wise & Abel 2005), and should be considered to accurately model future star formation.

BH formation in the death of some primordial stars can also have a profound effect on surrounding structure formation as it accretes infalling matter during later mergers. In principle, one should include feedback of seed BHs from primordial stars with masses outside of the range between 140 and 260 solar masses. Also it is possible to phenomenologically model SMBH formation in a similar manner as the stellar case. If the protogalactic collapse occurs faster than stellar formation timescale of a massive star, a SMBH may form inside this region. Using the stellar formation conditions plus this condition and allowing the particle to accrete (i.e. sink particles; Bate et al. 1995; Krumholz et al. 2004), protogalactic collapses can be followed in cosmological hydrodynamic simulations (Clark et al. 2007). These sink particles should regulate the accretion with an appropriate sub-grid model. Important processes include an appropriate accretion rate (e.g. Eddington or Bondi-Hoyle), turbulence (Krumholz et al. 2006), rotational support of the infalling gas, and a viscosity timescale for accretion discs.

For small galaxies, radiative transfer effects can have a great impact (e.g. Haehnelt 1995; Whalen et al. 2004; Kitayama et al. 2004; Alvarez et al. 2006) and should not be neglected. The promising approach of Gnedin & Abel (2001) has recently been implemented and coupled with the AMR hydrodynamic code ART (Gnedin et al. 2007). Also, the technique of adaptive ray tracing (Abel & Wandelt 2002) has been implemented into *Enzo* and used to study the outflows and ionizing radiation from a primordial star (Abel et al. 2007). This method has also been independently implemented into *Enzo* by Razoumov & Sommer-Larsen (2006). There ionization front instabilities create cometary small-scale structure and shadowing effects as a result from the explicit treatment of three-dimensional radiation hydrodynamics. Finally as used in many stellar formation routines (Cen & Ostriker 1992; Tassis et al. 2003), we hope to include thermal and radiative feedback from Population II stars in future studies.

5. CONCLUSIONS

We have simulated the hydrodynamics and collapse of a protogalactic gas cloud in two cosmology AMR realizations. Our focus on the hydrodynamics presents a basis for future studies that consider stellar and BH feedback. In the idealized case presented, we find a central dense object forms on the order of $10^5 M_\odot$ and $r \lesssim 5$ pc. This central object is not rotationally supported and does not

form fragment in our simulations. However our results do not dismiss disc formation in protogalaxies because rotationally supported disc formation may begin after the initial central collapse. However disc formation may be sensitively affected by feedback from the central object.

These simulations highlight the relevance of secular bar-like instabilities in galaxy formation and turbulent collapses. Similar bar structures are witnessed in primordial star formation simulations. As low angular momentum infalls, it gains rotational energy as it conserves angular momentum. This induces an $m = 2$, bar-like instability that transports angular momentum outwards, and the self-similar collapse can proceed without becoming rotationally supported and exhibits a density profile $\rho \propto r^{-12/5}$. This process repeats itself as material infalls to small scales that is indicative of the “bars within bars” scenario. We see three and four occurrences of embedded secular instabilities in the two realizations studied here.

We also find that supersonic turbulence influences the collapse by providing a channel for the gas to preferentially segregate according to its specific angular momentum. The low angular momentum material sinks to the center and provides the material necessary for a central collapse. Here the possibilities of a central object include a direct collapse into a SMBH (e.g. Bromm & Loeb 2003),

a starburst (e.g. Clark et al. 2007), or a combination of both (e.g. Silk & Rees 1998). All of these cases are viable in the early universe, and the occurrence of these cases depends on the merger history, local abundances in the halo, and the existence of a seed BH. Moreover, star formation should occur whether a central BH exists or not. Perhaps the frequency of these different protogalactic outcomes may be traced with either 3D numerical simulations that consider star and SMBH formation and feedback along with metal transport or Monte Carlo merger trees that trace Pop III star formation, metallicities, and BHs. We will attempt the former approach in future studies to investigate protogalactic formation in more realistic detail.

This work was supported by NSF CAREER award AST-0239709 from the National Science Foundation. We thank Kristen Menou, Michael Norman, Ralph Pudritz, Darren Reed, and Tom Theuns for helpful discussions. We applaud Greg Bryan and Michael Norman for developing an incredible code. We are grateful for the continuous support from the computational team at SLAC. We performed these calculations on 16 processors of a SGI Altix 3700 Bx2 at KIPAC at Stanford University.

REFERENCES

- Abel, T., Anninos, P., Zhang, Y., & Norman, M. L. 1997, *New Astronomy*, 2, 181
- Abel T., Bryan G. L., & Norman M. L., 2002, *Science*, 295, 93
- Abel, T., & Wandelt, B. D. 2002, *MNRAS*, 330, L53
- Abel, T., Wise, J. H., & Bryan, G. L. 2007, *ApJ*, 659, L87
- Alvarez, M. A., Bromm, V., & Shapiro, P. R. 2006, *ApJ*, 639, 621
- Anninos, P., Zhang, Y., Abel, T., & Norman, M. L. 1997, *New Astronomy*, 2, 209
- Bardeen, J. M., Friedman, J. L., Schutz, B. F., & Sorkin, R. 1977, *ApJ*, 217, L49
- Barnes, J., & Efstathiou, G. 1987, *ApJ*, 319, 575
- Bate, M. R., Bonnell, I. A., & Price, N. M. 1995, *MNRAS*, 277, 362
- Becker, R. H. et al. 2001, *AJ*, 122, 2850
- Begelman, M. C., Volonteri, M., & Rees, M. J. 2006, *MNRAS*, 370, 289
- Bertschinger, E. 1995, *ArXiv Astrophysics e-prints*, arXiv:astro-ph/9506070
- Bertschinger, E. 2001, *ApJS*, 137, 1
- Bonnor, W. B. 1955, *MNRAS*, 116, 351
- Bouwens, R. J., Ilingworth, G. D., Blakeslee, J. P., & Franx, M. 2006, *ApJ*, 653, 53
- Bromm, V., Ferrara, A., Coppi, P. S., & Larson, R. B. 2001, *MNRAS*, 328, 969
- Bromm, V. & Loeb, A. 2003, *ApJ*, 596, 34
- Bryan, G. L., Cen, R., Norman, M. L., Ostriker, J. P., & Stone, J. M. 1994, *ApJ*, 428, 405
- Bryan, G. L. & Norman, M. L. 1997, in *Computational Astrophysics*, eds. D. A. Clarke and M. Fall, ASP Conference #123
- Bryan, G. L. & Norman, M. L. 1999, in *Workshop on Adaptive Mesh Refinement Grid Methods*, IMA Volumes in Mathematics No. 117, ed. N. Chrisochoides, p. 165
- Bullock, J. S., Dekel, A., Kolatt, T. S., Kravtsov, A. V., Klypin, A. A., Porciani, C., & Primack, J. R. 2001, *ApJ*, 555, 240
- Burles, S., Nollett, K. M., & Turner, M. S. 2001, *ApJ*, 552, L1
- Cen, R. 2003, *ApJ*, 591, L5
- Cen, R. & Ostriker, J. P. 1992, *ApJ*, 399, 115
- Chandrasekhar, S. 1961, *Hydrodynamic and hydromagnetic stability*, Clarendon, Oxford
- Chandrasekhar, S. 1969, *Ellipsoidal Figures of Equilibrium*. Yale Univ. Press, New Haven
- Christodoulou, D. M., Shlosman, I., & Tohline, J. E. 1995a, *ApJ*, 443, 551
- Christodoulou, D. M., Shlosman, I., & Tohline, J. E. 1995b, *ApJ*, 443, 563
- Clark, P. C., Glover, S. C. O., & Klessen, R. S. 2007, *ApJ*, *submitted*, arXiv:0706.0613
- Couchman, H. M. P. 1991, *ApJ*, 368, L23
- Dekel, A., & Rees, M. J. 1987, *Nature*, 326, 455
- Ebert, R. 1955, *Zeitschrift für Astrophysics*, 37, 217
- Efstathiou, G. 1992, *MNRAS*, 256, 43P
- Eisenstein, D. J. & Hut, P. 1998, *ApJ*, 498, 137
- Eisenstein, D. J., & Loeb, A. 1995, *ApJ*, 443, 11
- Eisenstein, D. J., & Loeb, A. 1995, *ApJ*, 439, 520
- Endal, A. S., & Sofia, S. 1978, *ApJ*, 220, 279
- Fan, X., Narayanan, V. K., Strauss, M. A., White, R. L., Becker, R. H., Pentericci, L., & Rix, H. 2002, *AJ*, 123, 1247
- Fan, X., et al. 2006, *AJ*, 132, 117
- Ferrara, A. & Tolstoy, E. 2000, *MNRAS*, 313, 291
- Gardner, J. P. 2001, 557, 616
- Gnedin, N. Y. & Abel, T. 2001, *New Astronomy*, 6, 437
- Gnedin, N. Y., & Kravtsov, A. V. 2006, *ApJ*, 645, 1054
- Gnedin, N. Y., Kravtsov, A. V., & Chen, H.-W. 2007, *ApJ*, *submitted*, arXiv:0707.0879
- Greif, T. H., & Bromm, V. 2006, *MNRAS*, 373, 128
- Haehnelt, M. G. 1995, *MNRAS*, 273, 249
- Haiman, Z., Abel, T., & Rees, M. J. 2000, *ApJ*, 534, 11
- Haiman, Z., Rees, M. J., & Loeb, A. 1997, *ApJ*, 476, 458
- Helmi, A., et al. 2006, *ApJ*, 651, L121
- Hetzlnecker, H., & Burkert, A. 2006, *MNRAS*, 370, 1905
- Holmberg, E. 1941, *ApJ*, 94, 385
- Hoyle, F. 1949, in *Problems of Cosmical Aerodynamics*, ed. J. M. Burgers & H. C. van de Hulst (Dayton: Central Air Documents Office), 195.
- Hu, W. & Dodelson, S. 2002, *ARA&A*, 40, 171
- Jappsen, A.-K., Glover, S. C. O., Klessen, R. S., & Mac Low, M.-M. 2007a, *ApJ*, 660, 1332
- Jappsen, A.-K., Klessen, R. S., Glover, S. C. O., & Mac Low, M.-M. 2007, *ApJ*, *submitted*, arXiv:0709.3530
- Kitayama, T., Yoshida, N., Susa, H., & Umemura, M. 2004, *ApJ*, 613, 631
- Kolmogorov, A. N. 1941, *Dokl. Akad. Nauk SSSR* 30, 301 [Proc. R. Soc. London, Ser. A 341, 9 (1991)]
- Krumholz, M. R., McKee, C. F., & Klein, R. I. 2004, *ApJ*, 611, 399
- Krumholz, M. R., McKee, C. F., & Klein, R. I. 2006, *ApJ*, 638, 369
- Larson, R. B. 2003, *Reports of Progress in Physics*, 66, 1651
- Leibovitz, N. R. 1967, *ARA&A*, 5, 465
- Loeb, A., & Rasio, F. A. 1994, *ApJ*, 432, 52
- Lodato, G., & Natarajan, P. 2006, *MNRAS*, 371, 1813
- Lynden-Bell, D., & Ostriker, J. P. 1967, *MNRAS*, 136, 293
- Machacek, M. E., Bryan, G. L., & Abel, T. 2001, *ApJ*, 548, 509
- Maller, A. H., Dekel, A., & Somerville, R. 2002, *MNRAS*, 329, 423
- Mestel, L. 1963, *MNRAS*, 126, 553
- Mo, H. J., Mao, S. D. & White, S.D.M., 1998, *MNRAS*, 295, 319
- Mobasher, B., et al. 2005, *ApJ*, 635, 832
- O’Shea, B. W., Abel, T., Whalen, D., & Norman, M. L. 2005, *ApJ*, 628, L5
- O’Shea, B. W., Bryan, G., Bordner, J., Norman, M. L., Abel, T., Harkness, R., & Kritsuk, A. 2004, *ArXiv Astrophysics e-prints*, arXiv:astro-ph/0403044
- Oh, S. P., & Haiman, Z. 2002, *ApJ*, 569, 558

- Ostriker, J. P., & Bodenheimer, P. 1973, *ApJ*, 180, 171
 Ostriker, J. P., & Peebles, P. J. E. 1973, *ApJ*, 186, 467
 Ostriker, J. P., & Tassoul, J. L. 1969, *ApJ*, 155, 987
 Ostriker, J. P., & Gnedin, N. Y. 1996, *ApJ*, 472, L63
 Page, L., et al. 2007, *ApJS*, 170, 335
 Peebles, P. J. E. 1969, *ApJ*, 155, 393
 Peebles, P. J. E. 1971, *A&A*, 11, 377
 Peebles, P. J. E., & Dicke, R. H. 1968, *ApJ*, 154, 891
 Press, W. H. & Schechter, P. 1974, *ApJ*, 187, 425
 Press, W. H., & Teukolsky, S. A. 1973, *ApJ*, 181, 513
 Lord Rayleigh. 1920, *Scientific Papers*, 6, 447
 Razoumov, A. O., & Sommer-Larsen, J. 2006, *ApJ*, 651, L89
 Rees, M. J., & Ostriker, J. P. 1977, *MNRAS*, 179, 541
 Schneider, R., Omukai, K., Inoue, A. K., & Ferrara, A. 2006, *MNRAS*, 369, 1437
 Sheth, R. K. & Tormen, G. 2002, *MNRAS*, 329, 61
 Shlosman, I., Begelman, M. C., & Frank, J. 1990, *Nature*, 345, 679
 Shlosman, I., Frank, J., & Begelman, M. C. 1989, *Nature*, 338, 45
 Shu, F. H., Adams, F. C., & Lizano, S. 1987, *ARA&A*, 25, 23
 Shu, F. H. 1992, *Physics of Astrophysics, Vol. II*, (Sausalito: University Science Books)
 Silk, J., & Rees, M. J. 1998, *A&A*, 331, L1
 Smith, B. D., & Sigurdsson, S. 2007, *ApJ*, 661, L5
 Somerville, R. S. & Livio, M. 2003, *ApJ*, 593, 611
 Spaans, M., & Silk, J. 2006, *ApJ*, 652, 902
 Spergel, D. N., et al. 2003, *ApJS*, 148, 175
 Spergel, D. N., et al. 2007, *ApJS*, 170, 377
 Spitzer, L., Jr. 1978, *Physical Processes in the Interstellar Medium*, (New York: John Wiley & Sons), 143
 Stanway, E. R., Bunker, A. J., & McMahon, R. G. 2003, *MNRAS*, 342, 439
 Steinmetz, M., & Bartelmann, M. 1995, *MNRAS*, 272, 570
 Takizawa, M. 2005, *ApJ*, 629, 791
 Tassis, K., Abel, T., Bryan, G. L., & Norman, M. L. 2003, *ApJ*, 587, 13
 Thoul, A. A., & Weinberg, D. H. 1996, *ApJ*, 465, 608
 Tolstoy, E., Venn, K., Shetrone, M., Primas, F., Hill, V., Kaufer, A., & Szeifert, T. 2002, *Ap&SS*, 281, 217
 —. 2003, *AJ*, 125, 707
 Tolstoy, E., et al. 2004, *ApJ*, 617, L119
 Truelove, J. K., Klein, R. I., McKee, C. F., Holliman, J. H., Howell, L. H., & Greenough, J. A. 1997, *ApJ*, 489, L179
 Vitvitska, M., Klypin, A. A., Kravtsov, A. V., Wechsler, R. H., Primack, J. R., & Bullock, J. S. 2002, *ApJ*, 581, 799
 Whalen, D., Abel, T., & Norman, M. L. 2004, *ApJ*, 610, 14
 White, S. D. M., & Frenk, C. S. 1991, *ApJ*, 379, 52
 White, S. D. M. & Rees, M. J. 1978, *MNRAS*, 183, 341
 Wise, J. H., & Abel, T. 2005, *ApJ*, 629, 615
 Wise, J. H., & Abel, T. 2007, *ApJ*, 666, 899
 Woodward, P. R. & Colella, P. 1984, *J. Comput. Phys.* 54, 115
 Yoshida, N., Oh, S. P., Kitayama, T., & Hernquist, L. 2007, *ApJ*, 663, 687
 Yoshida, N., Omukai, K., Hernquist, L., & Abel, T. 2006, *ApJ*, 652, 6